Journal of Environmental Radioactivity 273 (2024) 107392

Contents lists available at ScienceDirect

Journal of Environmental Radioactivity

journal homepage: www.elsevier.com/locate/jenvrad

Using spectroscopic autoradiography of alpha particles for the quantitative mapping of ^{226}Ra ultra-traces in geo-materials

Hugo Lefeuvre [a,b], Sophie Billon [b], Michael Descostes [c,d], Jérôme Donnard [e], Samuel Duval [e], Paul Sardini [b,*]

[a] ERM (SARL), 7 rue Albert Turpain, 86000, Poitiers, France
[b] IC2MP – HydrASA, Poitiers University UMR, 7285, CNRS, France
[c] ORANO Environmental R&D Dpt, 125 Av. de Paris, 92320, Châtillon, Paris, France
[d] Centre de Géosciences, MINES ParisTech, PSL University, 35 rue St Honoré, 77300, Fontainebleau, France
[e] AI4R (SAS), 2 rue Alfred Kastler, Nantes, France

ARTICLE INFO

Keywords:
Alpha spectroscopy
^{226}Ra mapping
Uranium
Radioactive disequilibrium
Real-time autoradiography
Mining activities

ABSTRACT

The measurement of ^{226}Ra and the identification of ^{226}Ra-bearing minerals are important for studying the behavior of radium in the environment. Various instruments for measuring ^{226}Ra are currently used: among the radiometric techniques that measure in bulk (no spatialization), there are gamma spectrometers and alpha spectrometers. Other instruments such as SEM-EDS can map the chemical elements thus providing information on the distribution of ^{226}Ra, but are limited for ultra-trace analyses on natural geomaterials. Finally, autoradiography techniques can locate radioactivity, but are limited to the identification of the contribution of ^{226}Ra when the ^{238}U series is complete.

This study focuses on spectroscopic autoradiography, a method for measuring both the energy of the alpha particle emissions and their positions on the autoradiograph. A gas detector based on a parallel ionization multiplier technology was used for this purpose. Alpha particle energy is dependent on the emitting radionuclides. In order to track the ^{226}Ra, the energy spectrum of the ^{238}U series was studied with modeling software. It appears possible to apply a thresholding on the energy spectrum to discriminate the ^{226}Ra from the first alpha emitters of the ^{238}U decay chain (i.e. ^{238}U, ^{234}U and ^{230}Th, all below 5 MeV).

The developed method was applied to a U-mill tailing sample prepared as a thin section. The sample was heterogeneous in terms of radioactivity and was not at secular equilibrium with ^{238}U, as expected. The ^{226}Ra was identified and localized, and different regions of interest were also analyzed with SEM-EDS elements cartography. This revealed ^{226}Ra-rich barite ($BaSO_4$) phases measured at 3 ppm_{Ra} on average and containing no uranium; and uranium in siderite ($FeCO_3$), showing a strong ^{226}Ra deficit compared with secular equilibrium.

Spectroscopic autoradiography opens up possibilities for the analysis of heterogeneous geological samples containing natural alpha emitters such as ^{238}U and ^{226}Ra: the ^{226}Ra can be localized and quantified at ultra-trace content, and the method developed can also identify newly (young) uranium phases by measuring ^{238}U/^{226}Ra activity disequilibrium.

1. Introduction

^{226}Ra is the fourth alpha emitter of the ^{238}U decay chain. With a half-life of $T_{1/2} = 1600$ years, ^{226}Ra is naturally present in soils at an average concentration of 32 Bq/kg, i.e. about 1 ppt (UNSCEAR, 2010). It is one of the main NORMs (Naturally Occurring Radioactive Material) encountered in the environment but can also be encountered and released by various extraction industries (oil, shale gas, coal, phosphate and uranium mines) (INTERNATIONAL ATOMIC ENERGY AGENCY, 2010) (INTERNATIONAL ATOMIC ENERGY AGENCY, 2004) (World Health Organization, 1993) (Ahmad et al., 2021) (Jirásek et al., 2020) (Baetslé, 1991) (Ballini et al., 2020) (Chautard et al., 2020). ^{226}Ra is also known to be the radioactive decay father of ^{222}Rn, a volatile naturally-occurring radioactive noble gas.

The mobility of ^{226}Ra in the environment is mainly governed by water/rock interactions according to different retention processes at the water/mineral interface (mainly sorption onto clay minerals, metal oxy-

* Corresponding author. IC2MP, UMR 7285, B27, 4 RUE MICHEL BRUNET, TSA 51106, 86073, POITIERS Cedex9, France.
E-mail address: paul.sardini@univ-poitiers.fr (P. Sardini).

https://doi.org/10.1016/j.jenvrad.2024.107392
Received 8 November 2023; Received in revised form 19 January 2024; Accepted 24 January 2024

List of abbreviations

BSE	back-scattered electrons
EDS	energy dispersive spectrometer
EPMA	electron probe microanalyzer
FWHM	full width at half maximum
NORM	naturally occurring radioactive material
PIM	parallel ionization multiplier
ROI	region of interest
SA	spectroscopic autoradiography
SEM	scanning electron microscope
SIMS	secondary-ion mass spectrometry
TOF-SIMS	time of fly secondary-ion mass spectrometry
WDS	wavelength dispersive spectrometer

hydroxides, organic matter; or co-precipitation processes in SO_4- and CO_3- bearing minerals) (INTERNATIONAL ATOMIC ENERGY AGENCY, 2014) (Bordelet et al., 2018) (de Boissezon et al., 2020) (Leermakers et al., 2016) (Lestini et al., 2019) (Robin et al., 2017). The low elementary content of ^{226}Ra in soils and rocks can make the analyses complex and thus impact the understanding of ^{226}Ra mobility.

Several direct or indirect chemical and nuclear techniques are commonly used, but all are limited either in the spatial resolution or the detection limit of ^{226}Ra, and therefore do not allow a precise determination of the ^{226}Ra-bearing phases. Table S1 (supplementary) summarizes the detection limits, as well as the advantages and drawbacks of the different techniques for measuring ^{226}Ra.

Instruments based on elementary chemical analysis, such as the electron probe microanalyzer (EPMA) with X-ray analysis, scanning electron microscope with energy dispersive spectrometer (SEM-EDS) and wavelength dispersive spectrometer (WDS) (McGee and Keil, 2001), are also capable of mapping the chemical elements. With a high spatial resolution (1 μm (Cocherie et al., 1998)), their detection limit ranging between 100 and 1000 ppm is however not suitable for ultra-trace analysis such as for ^{226}Ra (Çubukçu et al., 2008) (Angileri et al., 2018). For higher concentrations, such as for natural uranium, chemical mapping is more appropriate and has the advantage of being non-destructive.

Among the mass spectrometers, the SIMS (secondary-ion mass spectrometry) can also provide information on the radium distribution (Rollog et al., 2020) (Becker, 2003). The possibility of imaging the radium is very interesting for making the association with its mineralogy, using complementary measurements by SEM. The detection limit of SIMS is about 1 ng/g, and its spatial resolution can approach 50 nm (Kollmer et al., 2013). The operating principle of SIMS is based on a local isotopic analysis, by focusing a primary-ion beam on a sample. Mass spectrometers and SIMS are used for both nuclear forensic and isotopic analysis (Song et al., 2016). The distribution of ^{226}Ra in barite at the 200 μm scale has been reported using the TOF-SIMS technique (Klinkenberg et al., 2014). The small mass-analysis geometry, the matrix effect on quantification, and difficult access to such apparatus can be disadvantages (Song et al., 2016).

The conventional methods for a bulk measurement of radium in geomaterials are alpha and gamma spectrometry. ^{226}Ra decays with alpha emissions at 4.784 MeV and to a lower intensity (3.6 %) with gamma emissions at 186.2 keV.

Alpha spectrometry offers good efficiency and a high signal-to-noise ratio, for example a detection limit of 0.6-0.1 mBq/g measured in sediments ((Tinker et al., 1995) (Hou and Roos, 2008)), which allows very low elementary concentrations down to the ppq to be detected. However, this technique often requires a rather elaborate preparation of the sample: in order to be able to interpret the alpha spectra, it is preferable to chemically separate the Ra by carrying out an active deposition in the form of a thin layer by electrodeposition on a metal disc (Mvondo et al., 2017) (Thakur et al., 2021). Gamma spectrometry has the advantage of being non-destructive, with minimal sample preparation. However, the standards must be in the same configuration and density as the samples. The detection efficiency is lower than that for alpha spectrometers (Tinker et al., 1995), which can lead to longer counting times. The same applies to the detection limit, which is a few orders of magnitude higher than that for alpha spectrometers (>50 mBq) (Hou and Roos, 2008). The superposition of the ^{235}U peak at 185.7 keV with the ^{226}Ra peak causes complications commonly encountered in the analysis of uranium rich samples (Thakur et al., 2021) (Déjeant et al., 2014).

Alpha-digital autoradiography has been investigated for the mapping and quantification of global alpha emissions in rocks using a parallel ionization multiplier (PIM) detector (Angileri et al., 2018) (Sardini et al., 2016) (Angileri et al., 2020), with measurements of ultra-trace concentrations (ppb) of radium in ^{226}Ra-doped celestine samples (Billon et al., 2020), and in more complex mixtures (Billon et al., 2024; Besançon et al., 2022). However, the samples in these two studies contained only ^{226}Ra and its radioactive daughters, which were partially in secular equilibrium with it. In this case, the radium mapping was directly and merely proportional to the local alpha count (in each pixel).

A more recent study on PIM detectors led to the development of a method called spectroscopic autoradiography (SA) (Lefeuvre et al., 2022). This work demonstrates the possibility of spatializing the alpha energy with a PIM detector during an alpha autoradiography measurement. The alpha energy is dependent on the emitting radionuclides.

The objective of this contribution is therefore to determine whether SA measurement with a PIM detector can be used to discriminate ^{226}Ra, in the form of quantitative mapping of low ^{226}Ra content in geomaterials, and potentially containing all or part of the ^{238}U and ^{235}U series radioisotopes. To do this, the daughters of ^{226}Ra that are in equilibrium are used, as they can be more easily discriminated by their high specific initial emission energies. The method associated with this selection is developed in the following section.

2. ^{226}Ra discrimination using Spectroscopic Autoradiography

2.1. Spectroscopic autoradiography using a PIM detector

The methodology developed herein is based on the real-time autoradiography of alpha and beta particles using the BeaQuant gas detector (Donnard et al., 2009a) (Donnard et al., 2009b) (Donnard et al., 2009c). Samples to be analyzed are prepared in the form of geological thin sections (a 30 μm thin section of geomaterial attached to a glass slide, with dimensions of 45 mm × 30 mm), preferably carbon-coated. The procedure is as follows. A sample is placed in a dedicated sample holder. The alpha particle count begins with the interaction of the alpha particles (emitting from the sample surface) with the gas: the gas atoms are ionized, creating primary electron/ion pairs along the path of the particles. The PIM structure of the detector, including parallel micro-meshes and a pixelated anode, allows the acceleration of the primary electrons with enough energy to ionize more atoms (here called the avalanche). Then, electrons drift to the pixelated anode and create a signal that enables the radioisotopes emitting the radioactivity from the thin-section surface to be localized. This gas-detector technology is advantageous for analysing large areas (up to 20 × 20 cm^2) with a good sensitivity (the background level count is 6.3 × 10^{-4} cps/mm^2 for alpha (Lefeuvre et al., 2022)).

The interactions of the alpha particles in the gas enable various measurements to be made, such as the energy deposited in the detector, and the length of the tracks. This allows the measurement of both the emission energy of the alpha particles and their position of emission (this duality of measurement is the SA). Not all events recorded by the machine are relevant for energy measurement, with only a small proportion (efficiency close to 4.4 %) of events being selected for reconstructing an energy spectrum (Lefeuvre et al., 2022). Some

characteristics of the SA were indeed measured such as the energy resolution of 7.3 % (~800 keV FWHM) for energies measured between 3 MeV and 9 MeV. However recent developments have improved the efficiency (Lefeuvre et al., 2022), which in the present paper is near 14.8 %. This improvement has been made possible thanks to the use of a supplementary assumption in the algorithm which sorts the particles (see supplementary S2). This change does not affect the measured energy spectrum. Note that the higher the efficiency, shorter the acquisition time will be, since counting uncertainties are linked to the square root of counts. A model (not described here) estimates that 2000 counts in the energy spectrum are sufficient to limit uncertainties due to the statistical effect, under optimal conditions.

However a new method is needed, to be able to select only the ^{226}Ra among the other emitters contributing to the energy spectrum of the alpha particles. Knowing that the source is relatively thick (30 μm of geomaterial) and that the energy resolution of the SA is poor (~800 keV FWHM at 4.6 MeV) compared to the resolution of silicon alpha spectrometers (semiconductor ~ 18 keV FWHM at 5.5 MeV (PIPS® Detectors Passivated Implanted Planar Silicon Detectors)), the conditions are not optimal for isolating ^{226}Ra from the bulk (degraded) spectrum. In other words, the low energy resolution of the energy spectrum obtained by the BeaQuant smoothes the staircases observed by classical alpha spectroscopy. The reconstruction of a source energy spectrum using simulation tools is needed to understand the energy signal and associate the alpha energy spectrum to a^{226}Ra count. The detection limit of alpha autoradiography using the BeaQuant is around 2 ppm for U at secular equilibrium (Sardini et al., 2016), and ppb of ^{226}Ra have already been measured (Billon et al., 2020). We expected to find a detection limit between 0.1 and 1 ppb of ^{226}Ra using SA.

2.2. Modeling and method development

To study the correlation between the alpha energy spectra and their ^{226}Ra counts we used AASI software, a code developed for simulating energy spectra in alpha spectrometry, based on the Monte-Carlo method (Siiskonen and Pöllänen, 2005). This software allows to specify different properties for the source and for the detector. The characteristics of the alpha detector (Canberra PIPS A450) were the following: silicon semiconductor, modelling diameter = 24 mm, energy resolution = 18 keV FWHM, thickness of the active volume = 200 μm, dead layer thickness = 0.05 μm. The source was positioned 12 mm from the detector.

2.2.1. Source model

The simulated source contained the ^{238}U series having the eight alpha emitters {^{238}U, ^{234}U, ^{230}Th, ^{226}Ra, ^{222}Rn, ^{218}Po, ^{214}Po, ^{210}Po} in secular equilibrium. Their initial emission energies ranged from 4198 keV to 7687 keV (Fig. 1). The source material was uraninite (UO_2) with a density of 10 g/cm^3. The geometry of the source was 30 μm thick, 32 mm in diameter.

The energy resolution of the simulated detector is configurable, and we used 18 keV FWHM (optimal resolution) and 800 keV FWHM (degraded resolution). The simulated spectra of the source are shown on Fig. 2 (E_0 is the emission energy of an alpha particle when leaving the source). Each spectrum of the different elements of the ^{238}U series is plotted separately, together with the measured sum. In the case of optimal energy resolution (Fig. 2A) the impulse response for one radionuclide is a staircase shape "falling" at the radionuclide's initial emission energy value. If the resolution is degraded (Fig. 2B), the impulse overflows beyond the initial emission energy value. Another aspect of the source is the proportion of alpha leaving the source-sample relative to alpha reaching the detector, which is influenced by the thickness of the source. This loss of efficiency is quantified by the F_E

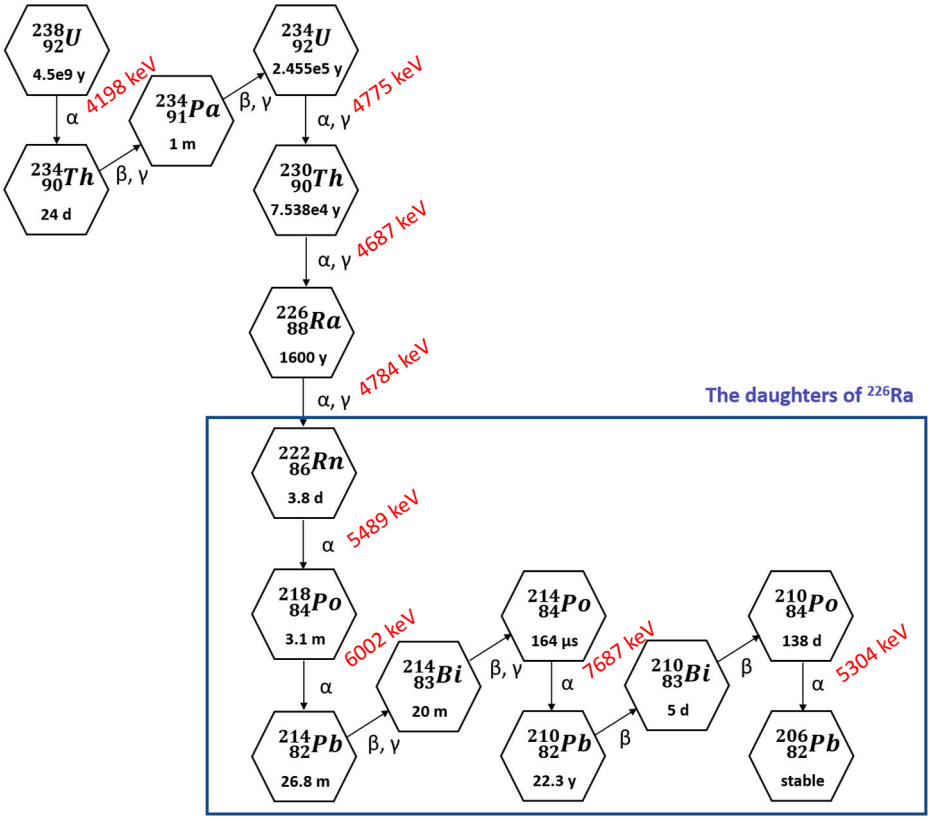

Fig. 1. ^{238}U series with corresponding alpha initial emission energies (in red). The ^{226}Ra daughters selected in the rectangle have the highest alpha emission energies (above 4784 keV, which is the emission energy of ^{226}Ra), reaching 6002 keV for ^{218}Po and 7687 keV for ^{214}Po.

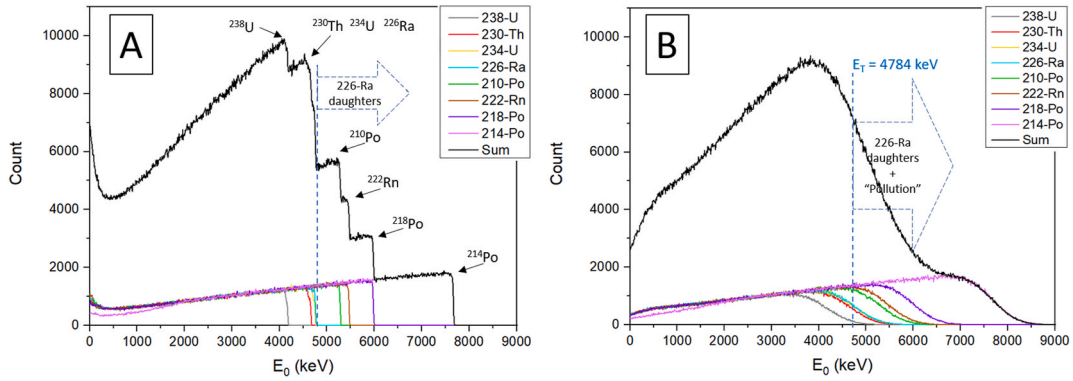

Fig. 2. Alpha energy spectrum of ^{238}U series; left (A) is the optimal energy resolution spectrum (18 keV FWHM) obtained by AASI simulations. Right (B) is the degraded energy resolution spectrum (800 keV FWHM) obtained from (A). The black distribution is the sum of the contributions of the eight radioelements. A threshold (E_T) is placed at 4784 keV on the energy spectra.

emission fraction (described in greater detail in (Billon et al., 2019)) estimated by sample simulation.

2.2.2. Energy thresholds and associated assumptions

The objective is to select the ^{226}Ra contribution (or proportion) from the alpha energy spectra of a thick source obtained with a degraded resolution (see Fig. 2 B). It is not possible to locate accurately the ^{226}Ra contribution in this degraded spectrum, because the peaks are not differentiable, in contrast to alpha spectroscopy of thin sources. Several assumptions and dedicated developments were therefore developed and are summarized in this section.

To locate ^{226}Ra, the assumption is made that ^{226}Ra is in secular equilibrium with its daughters, i.e. if A_x is the activity of radioelement x, then $\{A_{226Ra} = A_{222Rn} = A_{218Po} = A_{214Po} = A_{210Po}\}$. This assumption is valid at least for the first four radionuclides, because in this part of the decay chain, these radioisotopes each have a short half-life (Fig. 1). The case of ^{210}Po will be detailed separately (see section 2.3.2). Moreover, radon is a gaseous element and could well escape from the rock matrices. The radon loss must be prevented to reach radioactive equilibrium with ^{226}Ra. The problematic of ^{222}Rn will be emphasized in section 4.3. The daughter elements of ^{226}Ra selected in the rectangle on Fig. 1 correspond to the portion of the optimal energy spectrum above the value of 4784 keV (Fig. 2 A). Under these conditions, the counting rate of alpha particles having an emission energy higher than this value is proportional to the ^{226}Ra activity (in 4π sr). Considering the degraded energy resolution (Fig. 2 B), proportionality is not preserved with this energy threshold. The present study proposes to define in every spectrum (optimal or degraded) a proportionality (or conversion) factor k_8 between the net alpha count rate $N_{8\alpha}(E_0 > E_T)$ (count/s) for particles having an emission energy E_0 above a certain energy threshold E_T, and the total (in 4π sr) ^{226}Ra activity A_{Ra} (Bq) according to:

$$k_8(E_T) = \frac{A_{Ra}}{N_{8\alpha}(E_0 > E_T)} \quad (1)$$

It should be emphasized that $N_{8\alpha}$ represents a surface counting rate measured by SA in a given region of interest (ROI), whereas A_{Ra} is an activity (in 4π sr) related to the same ROI. A second $k_5(E_T)$ factor can be defined, where only the five radionuclides of radium and its daughters are considered for the calculation of $N_{5\alpha}$ (still with the same spectrum used to calculate k_8 and $N_{8\alpha}$):

$$k_5(E_T) = \frac{A_{Ra}}{N_{5\alpha}(E_0 > E_T)} \quad (2)$$

The k factor has been defined previously in a very general case. In the remainder of this section, the more specific case of secular equilibrium will be considered. In the case of the degraded spectrum, these k factors are renamed k_{8d} and k_{5d}. For different energy thresholds E_T, k_{8d} and k_{5d} vary not only in absolute value (Fig. 3 A), but also their associated error. Indeed, in the case of k_{8d}, the three ^{226}Ra parent elements {^{238}U, ^{234}U, ^{230}Th} can have reconstructed energies that exceed the threshold and therefore will be counted as contributing to ^{226}Ra alpha events (Fig. 2 B, degraded spectrum). The error associated with k_{8d} can be determined according to the threshold E_T thanks to an error $\xi\_k_{8d}(E_T) = (|k_{5d}\text{-}k_{8d}|/k_{5d}) \times 100$, where k_{5d} is taken as a reference value, because it does not take into account the pollution from the ^{226}Ra father elements.

The k_{8d} factor error as a function of the energy threshold E_T is plotted in Fig. 3 (B) for the case of a source where the whole ^{238}U series is at secular equilibrium. This error can be interpreted as the effect of a "pollution" of the ^{226}Ra fathers related to the energy resolution. With a threshold at 5200 keV the $\xi\_k_{8d} = 1$ %, however with a threshold at 6 MeV, it becomes negligible ($\xi\_k_{8d} = 0.01$ %).

The error introduced by the "pollution" of the ^{226}Ra fathers is not the only criterion for the choice of threshold. One must also be interested in the efficiency of the event selected by this threshold. In order to have a criterion on this proportion that does not depend on the instrument (but only on the spectrum) an efficiency ε_2 was defined (equation (3)): this corresponds to the number of alphas selected above the threshold E_T (integral of the spectrum above E_T), referred to as $N'_{5\alpha}(E_0>E_T)$ (i.e. only for Ra and daughter counts) with respect to all the alpha included in the measured energy spectrum N'_α (integral of the spectrum). The total energy spectrum count N'_α is limited between 3 MeV and 9 MeV according to the SA characteristic. Then we write:

$$\varepsilon_2(E_T) = \frac{N'_{5\alpha}(E_0 > E_T)}{N'_\alpha} x100 \quad (3)$$

This efficiency is calculated according to the threshold (E_T), always assuming that a degraded spectrum of a sample be at secular equilibrium (Fig. 4). The efficiency obviously decreases as the threshold increases. With a threshold fixed at 5500 keV the efficiency is 20 %, and the $\xi\_k_{8d} = 0.3$ % (and $k_{8d}(5500\text{ keV}) = 21.2 \pm 0.06$).

Another parameter that influences the general k_8 factor is the energy resolution of the detector. In the present paper, this resolution could change depending on the geometry of the detector or its internal technologies. For $E_T = 5500$ keV, the ξ_k_8 was plotted as a function of the energy resolution (see supplementary S3).

2.3. Impact of ^{238}U series disequilibrium on the measurement of radium

The simulations presented just above allowed a suitable energy threshold to be found for converting a surface counting rate to a ^{226}Ra activity (in 4π sr) in the sample, in the case of secular equilibrium. However, different radioactive disequilibria can be encountered in natural or anthropized samples, and are difficult to predict, requiring that the conversion factor be validated for different disequilibrium

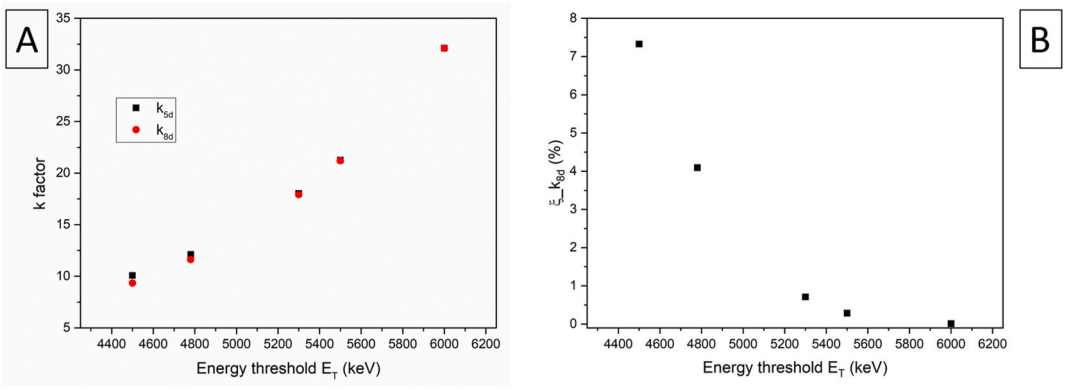

Fig. 3. For the degraded energy spectrum (source at secular equilibrium), k factors vs energy threshold (A) and ξ_k_{8d} vs energy threshold (B) calculated from the spectrum Fig. 2B.

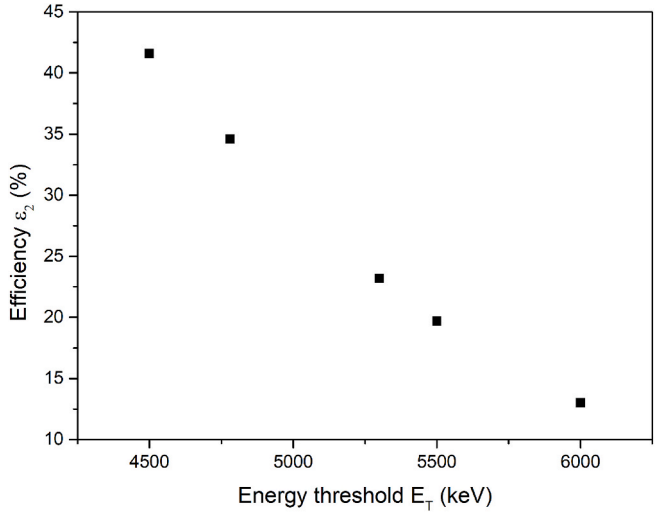

Fig. 4. Efficiency ε_2 of ^{226}Ra signal with respect to spectral signal vs threshold on energy spectrum (case of secular equilibrium and degraded spectrum).

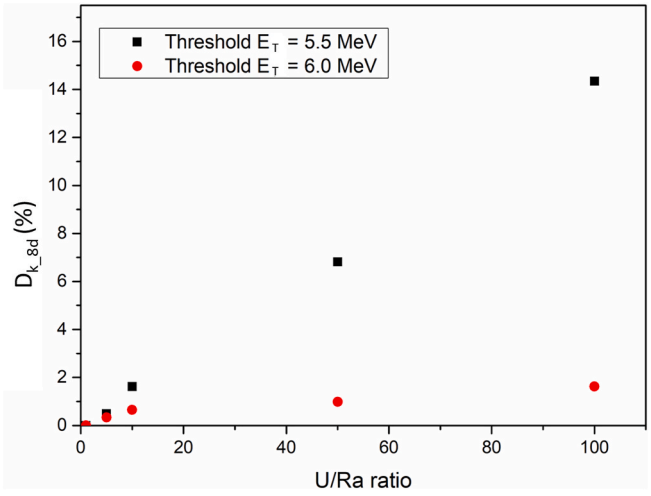

Fig. 5. Deviation of k_{8d}: $D_{k\_8d} = (k_{8d\_URa>1} - k_{8d})/k_{8d}$ vs U/Ra ratio (disequilibrium) at two different energy thresholds E_T.

states. It is therefore necessary to determine to what extent this disequilibrium can influence the measurement of radium with the method developed in the previous section. A disequilibrium corresponding to an excess of ^{226}Ra is referred to as U/Ra <1 and a disequilibrium with a shortage of ^{226}Ra is referred to as U/Ra >1.

2.3.1. *Cases of shortage (U/Ra >1) and excess (U/Ra <1) of ^{226}Ra*

Such disequilibria are associated with the following U and Ra alpha emitter groups: U group = {^{238}U, ^{234}U} and Ra group = {^{230}Th, ^{226}Ra, ^{222}Rn, ^{214}Po, ^{218}Po, ^{210}Po}.

A disequilibrium U/Ra = 0.1 was simulated using AASI (depletion in U). Using an energy threshold of 5500 keV, a $k_{8d\_URa0.1}$ of 21.22 was calculated (equation (1)). The relative difference (deviation) between $k_{8d\_URa0.1}$ and k_{8d} at equilibrium (21.2) is very low (0.11 %). In the case of a ratio U/Ra <1 the contribution of the U group in the calculation of k_8 is less than for an equilibrium state (U/Ra = 1). As there is less pollution, the deviation is necessarily small. The relative error on $k_{8d\_URa0.1}$ compared to a reference "$k_{5d\_URa0.1}$" is 0.033 %.

Furthermore, for an excess of uranium (U/Ra >1), the contribution of the U group to an alpha count having an emission energy higher than E_T increases with the U/Ra ratio. The deviation of k_{8d} defined as $D_{k\_8d} = 100 \times (|k_{8d\_URa>1} - k_{8d}|)/k_{8d}$ was determined for varying U/Ra ratios and for two E_T values (5500 keV and 6000 keV). As a reminder, k_{8d} is the value for secular equilibrium (when U/Ra = 1) and D_{k_8d} is plotted in (Fig. 5) for different U/Ra >1 values. When E_T = 5500 keV, D_{k_8d} varies linearly with the disequilibrium state, and non-negligible values are expected. D_{k_8d} stays below 2 % for U/Ra <10. It is still possible to decrease this deviation by being more restrictive on the threshold, using for instance E_T = 6 MeV (see red circles in Fig. 5). Under these conditions, D_{k_8d} is lower than 1.6 % for U/Ra <100. However, it is important to bear in mind that the efficiency ε_2 decreases when employing a higher threshold. At a threshold of 5.5 MeV, a large excess of uranium can generate a large deviation in k_8 (and thus on the quantification of the ^{226}Ra count), because the contribution of the U group to the emission energies higher than E_T becomes not negligible, and also because the radium content is small.

2.3.2. *Case of ^{210}Po*

Another disequilibrium to be studied is within the Ra group, between ^{226}Ra and ^{210}Po (which is at the end of the decay chain). This disequilibrium is generally observed for instance when ^{226}Ra is remobilized or when ^{222}Rn degasses. The time needed to find a stable activity (equilibrium) is about 200 years (~10 times the half-life of ^{210}Pb).

In the extreme case of total absence of ^{210}Po, the k_{8d_Po} (E_T = 5500 keV) = 21.74 (using equation (1)for a degraded spectrum, where the contribution of ^{210}Po was set to zero). The deviation relative to equilibrium $D_{k\_8d\_Po} = (k_{8d\_Po} - k_{8d})/k_{8d}$) is 2.5 %. After 22 years of closed system, half of the ^{210}Po radioactivity expected at secular equilibrium will be present, decreasing this deviation to 1.3 %. Finally, the impact of ^{210}Po equilibrium is also considered as negligible for quantifying the radium, because when counting alpha having emission energy higher

than 5500 keV, the area corresponding to the ^{210}Po alpha count alone is small compared to the sum of the other four alpha emitters of the Ra group. Indeed, the energy emission of ^{210}Po (5304 keV) is slightly lower than the chosen energy threshold of 5500 keV.

2.4. Samples

The first studied sample is a U ore sample in the form of a thin section (thickness 30 μm), which comes from the Cigar Lake mine site (Canada). The ore deposit is part of the Athabasca Basin and is located approximately 430 m below the surface. It was formed by three stages of U mineralization (from the three major fluid events), and the youngest event is estimated to be at least 19 Ma ago by U–Pb chemical dating (Fayek et al., 1997). The U mineralization consists mainly of uraninite, with accompanying coffinite, in a clay-rich matrix dominated by illite and chlorite. The average uranium content of the samples is high (around 15.9 %) and can reach up to 30 %. Considering the age of the deposit, the elements of the ^{228}U series are at secular equilibrium.

The second sample is made of ^{226}Ra-doped celestine ($SrSO_4$). It was obtained by crushing a natural centimetric-size celestine monocrystal, resulting in grain sizes ranging from 200 μm to 1 mm (described as "sample S3" in (Billon et al., 2020)). These fragments of celestine, initially not radioactive, were immerged in a ^{226}Ra spiked solution for 25 weeks. Dissolution/recrystallization processes took place on the grain surfaces, allowing the incorporation of ^{226}Ra in the celestine crystal lattice ([Ra–Sr]SO_4 solid solution). The crystal fragments were then embedded into epoxy resin. Gamma spectrometry was performed to measure ^{226}Ra mass activity (or specific activity) Am_{Ra} = 6410 Bq/g (256.4 Bq for 0.04 g). Using alpha spectroscopy, ^{226}Ra was found to be at secular equilibrium with ^{222}Rn, ^{218}Po, and ^{214}Po, but the ^{210}Po was not at secular equilibrium with ^{226}Ra and its daughters. The proportion of ^{210}Po was measured at 35 % of the equilibrium state (Billon et al., 2020). This sample was used by (Billon et al., 2020) to map and quantify ^{226}Ra by alpha autoradiography; for this material, alpha mapping was simply proportional to ^{226}Ra content, as ^{226}Ra and its progeny were the only alpha emitters present.

The third studied sample, depleted in uranium, referenced 9693-3, is a mill tailing coming from the former uranium mines exploited by COMUF in Gabon (Billon et al., 2024). Previous mineralogical analysis described a composition mainly of quartz, feldspars, mica/illite, chlorite and kaolinite and many accessory minerals like siderite, Fe and Ti oxides, and sulfate- or sulfide-bearing minerals. The site is now remediated and is under radiological and environmental monitoring. Concentration activities of 55.5 Bq/g for ^{226}Ra and 103 Bq/g for ^{230}Th have been measured by gamma spectroscopy bulk measurement. ^{238}U have been measured at 336 ppm by bulk analysis (~4 Bq/g). This sample is more complex than the other two, because it is neither in secular equilibrium ^{238}U, nor supposed to contain only ^{226}Ra and daughters. Moreover, it is mineralogically heterogeneous. It is therefore studied more carefully by microscopy to try to determine the ^{226}Ra content of the mineral phases of interest. The studied carbon-coated thin section 9693-3 was observed using a scanning electron microscope (SEM) (JEOL type JSM-IT500, IC2MP at Poitiers University). The observations were performed in the back-scattered electrons (BSE) imaging mode using the following conditions: acceleration voltage 15 kV, probe current 1 nA, working distance 11 mm. The SEM was coupled with a Bruker QUANTAX energy dispersive spectroscopy (EDS) X-ray analyzer (resolution <125 eV for X-Rays) allowing chemical analyses with a counting time of 40 s.

3. Calibration and samples analysis

3.1. Calibration of k_8 factor with the U ore sample

The thin slide was positioned in a custom-made sample-holder, then placed inside the detector chamber. The acquisition time was 37074 s (~10 h). A counting rate of N = 190.0 cps was measured on the bulk autoradiography image. The measured counting rate corresponding to the contribution of the eight alpha emitters of the ^{238}U series. It was possible to calculate the Ra activity (A_{Ra}), because at secular equilibrium the proportion of alpha particle emissions is the same for each of the eight emitters. Therefore, the counting rate of ^{226}Ra alone is N_{Ra} = 23.75 cps (1/8 of N). The alpha particles coming from the source surface were detected with a detection internal efficiency ε = 80 % (Sardini et al., 2016). The activity in 4π sr which takes into consideration the space volume of detection (2π sr) and the alpha particles stopped inside the sample itself (estimated by simulation), lead to an emission fraction F_E = 25 % (Billon et al., 2019) if the thickness of the source is considered as higher than the range of alpha particles in the source. The relationship between the ^{226}Ra activity in the source and the ^{226}Ra counting rate of the autoradiography is $N_{Ra} = A_{Ra} \times \varepsilon \times F_E$; the value of ^{226}Ra activity was found to be A_{Ra} = 118.75 Bq for the ore sample.

The alpha energy spectrum was measured using the SA method, and plotted in red on Figure S4 (A). It is compared with the alpha spectrum of the ore sample at secular equilibrium (in blue) acquired at the higher detector resolution, however for comparative purposes the resolution of the blue spectrum has been degraded histogram. By counting all the events after the energy threshold (E_T = 5500 keV) on the red spectrum, the total bulk count $N_{8\alpha}$ = 6.13 cps. Finally, the k-factor can be calculated according to equation (1), leading to k_8(5500 keV) = 19.4.

3.2. Determination of the k_8 factor with the celestine-Ra sample

Another possibility for calculating the k_8 factor of the PIM detector is to use a sample with a known ^{226}Ra content, such as ^{226}Ra-doped celestine. The activity (Bq, in 4π sr) for alpha of the ^{226}Ra-doped celestine sample A_{Ra} can be deduced from its mass activity Am_{Ra} measured by gamma spectrometry (see section 2.4). The alpha particles are emitted in an effective grain volume $V_{eG} = 2.20 \times 10^{-4}$ cm^3 (Billon et al., 2020). Given a density of $\rho = 3.95$ g/cm^3, the corresponding mass is m = 8.69 $\times 10^{-4}$ g, and the corresponding alpha particle activity for ^{226}Ra in this volume is A_{Ra} = 5.57 Bq in the whole section (with $A_{Ra} = Am_{Ra}$. m).

The energy spectrum of the celestine sample measured with SA after an acquisition time of 432377 s (~5 d) is plotted in red on Figure S3 (B). By applying the energy threshold at E_T = 5500 keV, the ^{226}Ra counting flux of $N_{8\alpha}$ = 0.285 cps is measured with the SA. This gives a k-factor for radium quantification k_8(5500 keV) = 19.5 with the celestine-Ra sample.

Another method to obtain the A_{Ra} activity value is the same as the one used for the ore sample (see section 3.1): using the autoradiography bulk counting rate and the knowledge of radionuclide activity efficiency. A counting rate of N = 6.7 cps was measured on the bulk autoradiography image. For the ^{226}Ra-doped celestine, the contribution of ^{226}Ra is not 1/8 (as for the ore sample) but is 1/4.35 according to the alpha spectroscopic measurement (section 2.4). The radium counting rate is therefore N_{Ra} = 1.54 cps (1/4.35 of N). Then, by applying the efficiency ε and the emission fraction F_E, the ^{226}Ra activity is A_{Ra} = 7.7 Bq. This second method leads to a calculation of k_8(5500 keV) = 26.6 (according to equation (1)).

The calculation of k_8 is preferred according to the first method applied on the celestine sample, as there are fewer intermediary efficiency factors and therefore fewer potential sources of errors. The ^{226}Ra doped celestine can be used as a standard for the measurement and for the quantification of ^{226}Ra activity, with k_8 = 19.5 for the PIM detector and by using an energy threshold E_T = 5500 keV.

3.3. Quantitative mapping of ^{226}Ra for the U-mill tailing sample

3.3.1. Quantitative mapping of ^{226}Ra

Alpha autoradiography of the 9693-3 sample was performed with the BeaQuant system (PIM detector) under the same conditions as for the ore and the ^{226}Ra-doped celestine sample (same sample-holder, same sample position). The thin section (30 μm thick, 45 × 30 mm^2) was

carbon coated to make it conductive, in order to act as a cathode inside the detector. The result of the autoradiography is shown in Fig. 6 (A), in the form of a radioactivity count at the surface. The acquisition time to obtain the image was 612007 s (about 7 days), and the surface counting rate of alphas was N = 3.44 cps. The alpha energy spectrum corresponding to the radioactivity was also measured with the PIM detector by applying the SA method (Lefeuvre et al., 2022). This energy spectrum is displayed in red on Fig. 6 (B) and corresponds to the bulk spectrum. It is compared to a spectrum from an alpha chamber (in blue on Fig. 6 (B)) measured with a Canberra semiconductor whose energy resolution has been post-treated by convolution using a Gaussian filter. This comparison also allows the energy measurement of the PIM detector to be calibrated (see (Lefeuvre et al., 2022)). The red spectrum shows overcounting at an energy below 3800 keV, due to the reconstruction method.

For the first step, the developed method was directly applied to measure the bulk ^{226}Ra activity (A_{Ra}) with the PIM detector. It was determined by the total count rate after the energy threshold (5.5 MeV) in the red spectrum, multiplied by the k_8 conversion factor (19.5) calculated with the ^{226}Ra-celestine sample (described in paragraph 3.2). A bulk ^{226}Ra activity of 2.40 Bq was determined for the whole sample.

Next, the combination of the spectral measurement modality and the autoradiography from the PIM detector was employed to map the spatial distribution of ^{226}Ra. Firstly, this spatialization was performed by selecting only those autoradiography events (or alpha counts) that were above the energy threshold of 5500 keV (^{226}Ra and descendants), creating a radium map. Secondly, by means of a calibration measurement, this radium map of surface counts was converted point-by-point into a real ^{226}Ra activity map in Bq of each pixel of the section, by dividing the counts by the acquisition time and multiplying by the k_8 factor. The result of the ^{226}Ra mapping is shown on Fig. 7 using a 50 μm pixel size.

The characterization of the distribution of ^{226}Ra with respect to father elements such as uranium was investigated in section 3.3.2. For that, the total count selected in the whole range of the alpha energy spectrum was utilised (i.e. not only the count after the energy threshold).

3.3.2. *Proportion of ^{226}Ra to other alpha emitters*

A map comparing the proportions of the activities of all the alpha emitters on the one hand and ^{226}Ra on the other hand, is proposed by combining two maps.

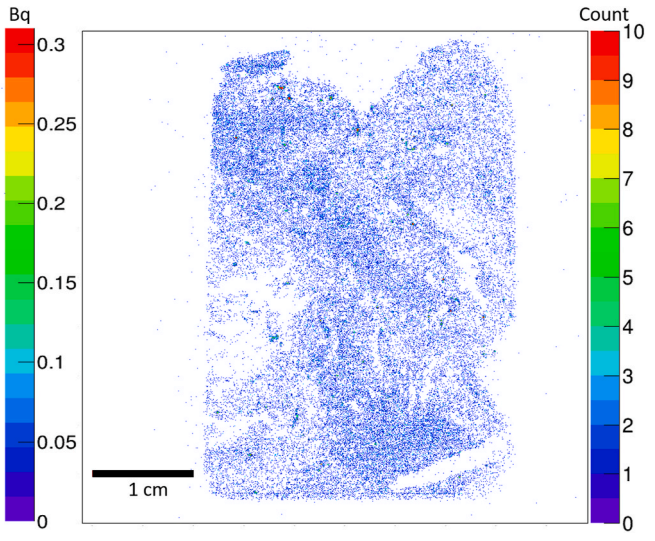

Fig. 7. ^{226}Ra quantitative map for the 9693-3 sample in Becquerel scale (^{226}Ra activity (4π)) and in count scale (^{226}Ra and descendants counts are proportional with ^{226}Ra) using the BeaQuant PIM detector

- Map 1 The ^{226}Ra map called “Ra”, obtained by a threshold at 5.5 MeV on the energy spectrum, i.e. following the method previously described (Fig. 7).
- Map 2 The map of all alphas found in the energy spectrum between 3 MeV and 9 MeV, in order to obtain a count which is the sum of the U and Ra groups, called “TOT” (Fig. 8).

The point-by-point division of these two maps Ra/TOT provides information on the proportion of radium activity in relation to the other elements (especially with U), i.e. the disequilibrium state. Before dividing the two maps, a convolution filter (3x3 kernel {0, 1, 0}, {1, 2, 1}, {0, 1, 0}) was applied to each map, allowing the alpha distributions to be diffused in order to fill the empty pixels. This new map is called "Ra/TOT map". The result is plotted in Fig. 8 (A) for the 9693-3 sample. The count ratio measured in each image pixel (50 μm) is then of value

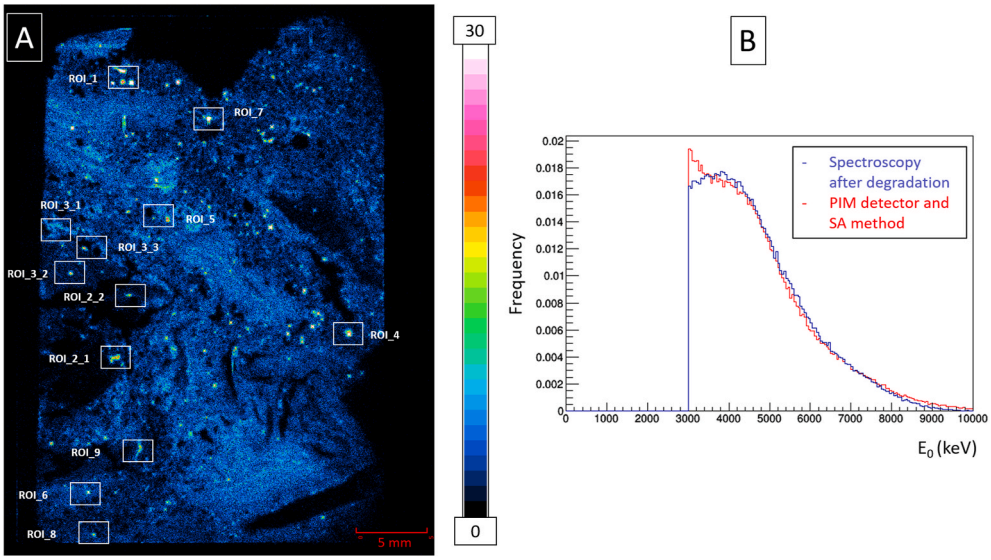

Fig. 6. (A) Autoradiography of 9693-3 sample with PIM detector (open in Beamage software). The color scale (right) indicates the net count in each pixel (pixel size 30 μm). (B) alpha energy spectrum for the same sample, with PIM detector (in red) and alpha spectroscopy chamber (in blue). The two spectra are normalized by their integral. The different regions of interest (ROIs) studied below are shown in (A) using rectangles.

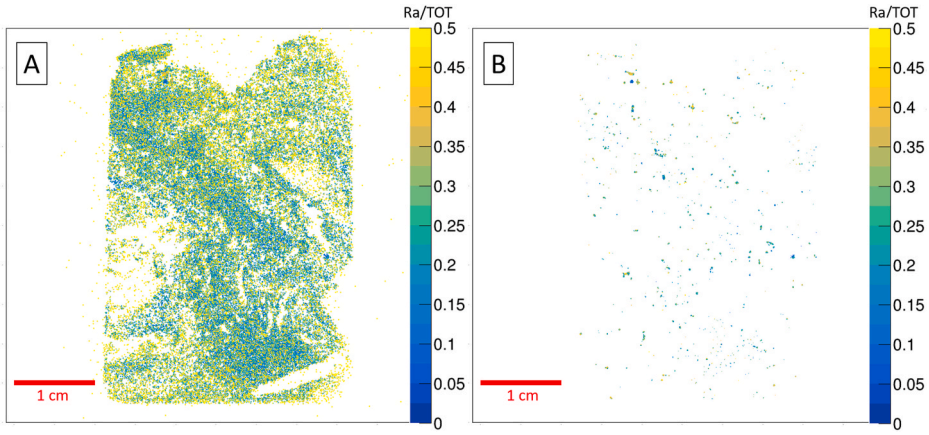

Fig. 8. Ra/TOT map for 9693-3 sample, (A) with no restriction on counts in Ra and TOT counting; (B) by selecting only pixel with count > 4 on TOT with energy between [3,9] MeV.

Ra/TOT <1 (with a theoretical maximum value close to Ra/TOT = 0.3: it may however be higher because of the poor statistic of the counting in some pixels of (1) and (2) map). Theoretical values of Ra/TOT can be predicted thanks to the modeling for the degraded spectrum and for different disequilibrium states: Ra/TOT = 0.24 at secular equilibrium of ^{238}U; Ra/TOT = 0.05 when only ^{238}U and ^{234}U are present; Ra/TOT = 0.30 when only ^{226}Ra and 4 daughters are present; Ra/TOT = 0.27 in the case of an equilibrium from ^{230}Th to ^{210}Po.

The Ra/TOT map enhances some contrasts between Ra and other emitters (of the U group) in different areas that can be selected for supplementary analysis. To avoid the background due to a poor statistical count and to easily identify regions of interest, a limit was applied on the TOT map to select and display only pixels above 4 counts (see Fig. 8 B). Pixels having a value lower than 4 counts are masked in white in Fig. 8 B.

3.3.3. *Determination of the Ra- and U-bearing mineral phases of the different ROI*

3.3.3.1. Analysis of ROI_1. The region of interest labelled ROI_1 (on Fig. 6 A), which defines an area of 3.2 × 2.4 mm^2, was observed with the SEM and then compared to the alpha autoradiography to determine the mineral phases carrying the different radioactive signals (see Fig. 9(A) and (B)).

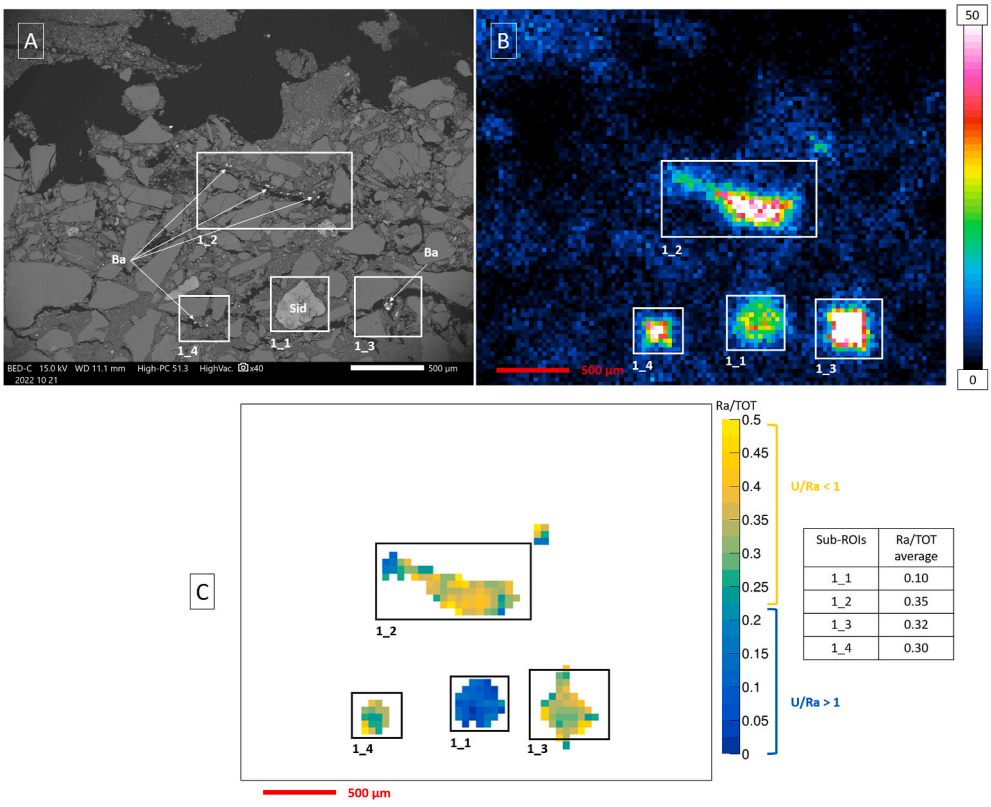

Fig. 9. Analysis in ROI_1: in SEM, BSE mode, some small barites (Ba) are indicated with arrows (A), by autoradiography of all alpha (B), and by Ra/TOT map (C) where the contrast in blue is disequilibrium U/Ra > 1 (U alone) and the signal in yellow is U/Ra < 1 (enriched in ^{226}Ra). The Ra/TOT average of each sub-ROIs is calculated and given in the table. Sub ROI_1_1 corresponds to a siderite grain, while sub-ROIs 1_2, 1_3 and 1_4 correspond to small grains of barite that appear in white in SEM-BSE image (and showed with white arrows).

Four sub-ROIs of radioactivity emission referred to as 1_1, 1_2, 1_3, and 1_4 were identified. EDS point analyses were used to identify the following mineral phases: barite ($BaSO_4$) (grain size ~ 5 μm) in 1_2 and 1_4; slightly larger barite for 1_3 (grain size ~ 45 μm), barite in every case being associated with the organic matter phase (continental plants). The mineral in 1_1 (~300 μm) consists of siderite ($FeCO_3$) (concretional shape), and a local EDS measurement performed at the edges of the siderite concretion showed inclusions of P (2.1 %), Pb (19.1 %), S (2.3 %), V (11.2 %), and U (1.1 %). Note that the distributions of radioactivity on the autoradiography appear wider than the size of the bearing mineral phases observed with SEM: this is due to the lower spatial resolution of autoradiography compared to SEM (depending mainly on the alpha range), and also on the fact that SEM and autoradiography do not probe the same sample volume. The interaction volume of SEM is below the μm^3 scale, while alpha particles emitted from a depth of about 25 μm can be detected at the surface. Therefore some minerals below the sample surface (not observed on the SEM picture) can provide a signal on an autoradiography image. This is particularly true for small crystals such as barite (5 μm).

Information on the proportion of ^{226}Ra compared to the other emitters of the series is well illustrated in Fig. 9 (C) using the Ra/TOT map. There is an observed inhomogeneity between the sub-ROIs. In zone 1_1 the ratio Ra/TOT = 0.10 appears distinctly lower than the three others (Ra/TOT >0.30). The ^{226}Ra content is indicated in Table 1 (see below).

3.3.3.2. Analysis of ROI_2_1. Fig. 10 highlights the SEM and autoradiography analysis of ROI 2_1 (this ROI is localized in Fig. 6 A). ROI_2_1 is another example presenting small barite grains (average size ~ 5 μm) near the organic phase visible on Fig. 10 (C, D). The quartz (visible on Fig. 10 (A, B)), being not radioactive, facilitates the localization of the autoradiography with SEM images. The average signal of the ratio Ra/TOT = 0.30 is also comparable to 1_2, 1_3 and 1_4 ROIs (see Table 1).

3.3.3.3. Analysis of ROI_3_1. Fig. 11 shows the analysis of ROI_3_1 (and this ROI is localized in Fig. 6 A). For ROI_3_1, the signal is more dispersed than for the previous ROIs and the activity level is lower. Siderite cement, highlighted by iron content on the EDS chemical map (yellow on Fig. 11 B), appears correlated to the autoradiography signal outlined in white in Fig. 11 (D). The presence of V (1.3 %), P (1.1 %) and S (0.6 %) inclusions is also notable, but in lower concentrations than for 1_1 Sub-ROI. The Ra/TOT measurement on Fig. 11 (C) for this siderite-bounded contribution outlined in black is 0.12. The U content is measured at 2.2 wt % locally.

3.3.3.4. Analysis of ROI_4. The results of the following ROI_4 analysis are shown in Fig. 12. The ROI_4 zone is interesting because it combines the two possibilities seen before of superimposing the barite and siderite visible on the SEM image in Fig. 12 (A, C) on the same spot. The smaller barite emits a "strong" autoradiography signal around the larger siderite (Fig. 12 (B)). The interpretation of the autoradiography signal is more difficult in this case, and Ra/TOT = 0.17 is measured in this spot ((Fig. 12 (D)).).

3.3.4. Generalized analyses in several ROIs

The study of all the ROIs highlighted in Fig. 6 (A) was also generalized, i.e. 15 areas were analyzed, the results being summarized in Table 1.

The estimation of the ^{226}Ra concentration in the mineral phases (column 6, Table 1) of each ROI requires the identification of those minerals. The mass of material corresponding to barite and siderite was calculated from the SEM backscatter images. The atomic number Z of

Table 1
Analysis of radium content in the 9693-3 sample (with SA method measurement) and of uranium content in different ROIs. The uncertainty in the ^{226}Ra content measurement (in ppm) was calculated with statistical uncertainty (sqrt(N) on the N_{Ra} measured).

ROIs	Total alpha count (c/s) in Autoradiography	Ra count with SA (N_{Ra} x time)	TOT count in spectrum (with SA)	Surface area (μm^2) (SEM)	^{226}Ra content (ppm) (with SA)	^{226}Ra mass activity (Bq/g) (with SA)	Mineral phases (EDS)	Ra/TOT (SA)	U (%) (EDS)
Bulk	3.44	75317	315781	8.9×10^8	$1.42 \pm 0.004 \times 10^{-3}$	52 ± 0.02	ρ mean 2.35 g/cm^3	0.24	–
1_1	3.69×10^{-3}	37	353	62206	$5.87 \pm 1 \times 10^{-3}$	218 ± 36	Siderite	0.10	1.1 %
1_2	8.83×10^{-3}	368	1048	1337	2.40 ± 0.1	89026 ±4641	Barite	0.35	–
1_3	1.14×10^{-2}	413	1271	1531	2.35 ± 0.1	87252 ±4293	Barite	0.32	–
1_4	2.42×10^{-3}	71	234	132	4.69 ± 0.6	173974 ±20647	Barite	0.30	–
2_1	6.31×10^{-3}	202	677	402	4.38 ± 0.3	162527 ±11435	Barite	0.30	–
2_2	1.73×10^{-3}	73	244	98	6.50 ± 0.8	240933 ±28199	Barite	0.30	–
3_1	1.23×10^{-2}	104	820	120259	$7.55 \pm 0.8 \times 10^{-3}$	280 ± 27	Siderite	0.13	2.2 %
3_2	2.33×10^{-3}	67	245	283	2.06 ± 0.3	76575 ±9355	Barite	0.27	–
3_3	2.10×10^{-3}	57	204	304	1.63 ± 0.2	60646 ±8033	Barite	0.28	–
4	8.32×10^{-3}	124	705	–	–	–	Siderite + Barite	0.17	0.67 %
5	4.22×10^{-3}	46	287	70300	$6.46 \pm 1 \times 10^{-3}$	239 ± 35	Siderite	0.16	0.8 %
6	2.39×10^{-3}	92	288	104	7.72 ± 0.8	286124 ±29831	Barite	0.32	–
7	1.44×10^{-2}	522	1504	3557	1.28 ± 0.06	47454 ±2077	Barite	0.35	–
8	1.08×10^{-3}	62	169	2043	0.266 ± 0.04	9816 ±1247	Barite	0.37	–
9	3.83×10^{-3}	156	583	1374	0.10 ± 0.08	36723 ±2940	Barite	0.27	–

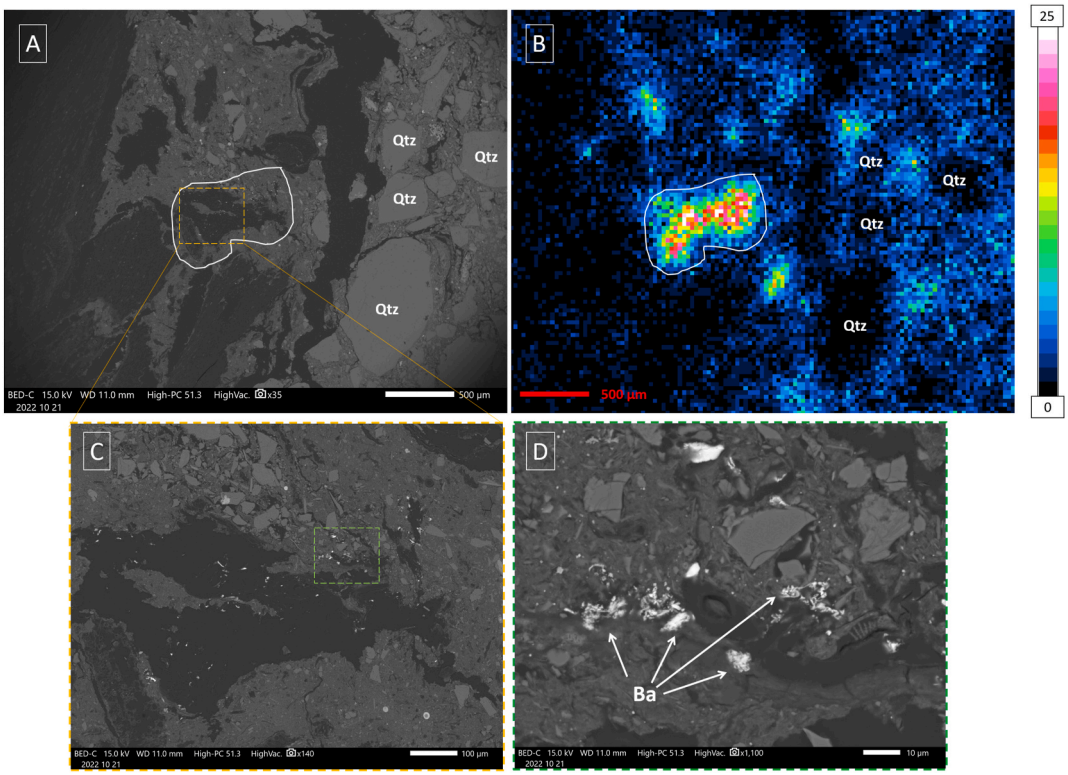

Fig. 10. Analysis of ROI_2_1 (see Figure 6) in SEM, BSE mode (A), by autoradiography of all alpha (B), in SEM, BSE magnified for observing small barite grains (C), zoom on barites (Ba) identified in white contrast on SEM image (D). (C) is a magnification of the yellow rectangle area presented in (A), and (D) is a magnification of the green rectangle area presented in (C).

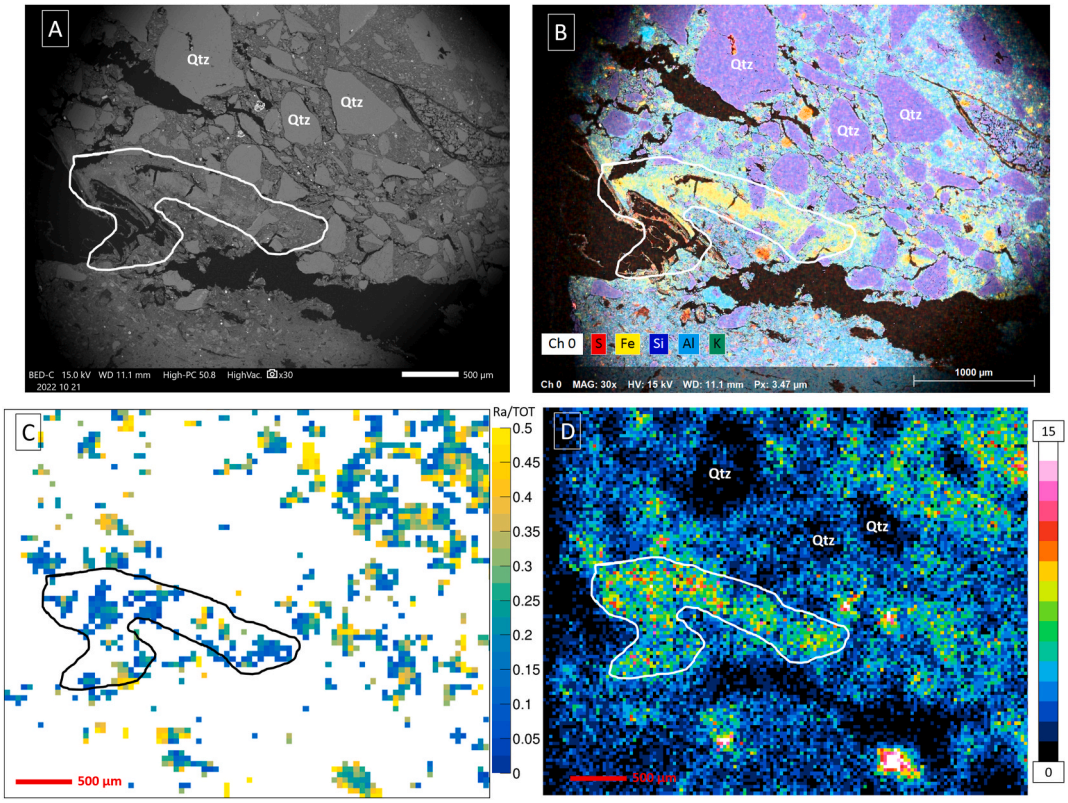

Fig. 11. Analysis of ROI_3_1 showing siderite as alpha emitter: SEM image in BSE mode (A), SEM-EDS chemical map (B), Ra/TOT map (C), Autoradiography of all alpha (D). The siderite is not easily identified in BSE mode because it occurs as cement between the grains, but siderite is highlighted in EDS map by the presence of Fe, displayed in yellow colour.

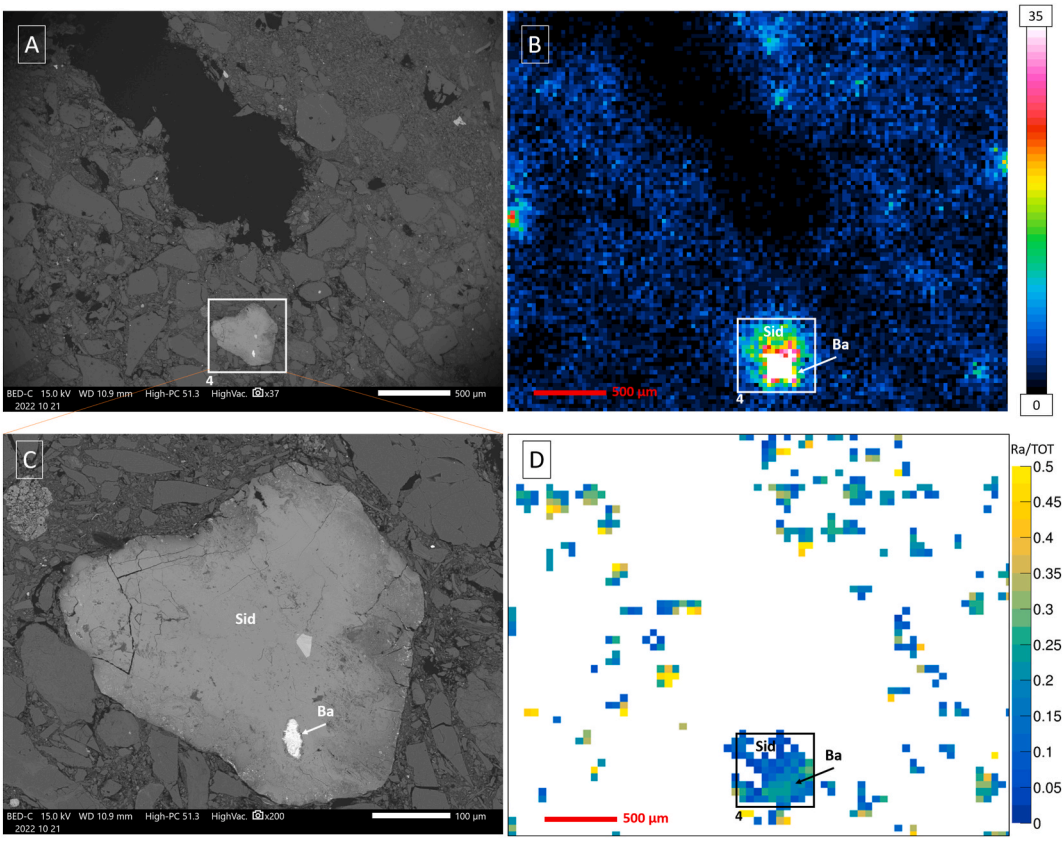

Fig. 12. Analysis in ROI_4: SEM, BSE mode (A), autoradiography of all alpha, barite (Ba) is associated with a strong alpha radioactivity signal, while siderite (Sid) indicates a weak signal (B), SEM image zoom on the spot with siderite (Sid) and barite (Ba) included into the siderite (C), Ra/TOT map; the contrast between siderite (Sid) and barite (Ba) is visible despite superimposing them on the same spot (D).

the elements is proportional to the grayscale level of the SEM image, allowing a threshold to be set and the mineral of interest to be isolated. Then the surface area of the mineral was calculated using ImageJ (ImageJ) software (see supplementary S5 for an example). The thickness of the effective active volume was fixed at 22 µm which corresponds to the average ranges of the alpha particles detected for the ^{226}Ra measurement; and the mass of material is the calculated volume multiplied by the density of the phases. The average ^{226}Ra content in barite-ROIs is 3.1 ppm, and the average ^{226}Ra content in siderite is 6.6 ppb. The ^{238}U concentration (column 10, Table 1) was measured with the EDS probe of the SEM.

For the measurement of bulk ^{226}Ra, a concentration of 1.42 ppb of the whole section of the sample 9693-3 was found. This value is the bulk ^{226}Ra activity (2.40 Bq, see section 3.3.1) divided by the mass (m) of the sample (and then converted into ppb). The mass of the sample was estimated based on an average calculation of the density ρ_mean = 2.35 g/cm^3 and the porosity from the SEM measurements (see supplementary S6). The volume of the sample was estimated for an effective thickness of 22 µm and the porosity was subtracted from the volume. This gave mass m = 46.0 mg, and mass activity was calculated as 52 Bq/g.

4. Discussion

A previous study has highlighted the possibility of using the PIM detector to quantify ^{226}Ra in celestine samples (Billon et al., 2020). The objective of the present study is to be able to quantify ^{226}Ra in a section of geo-materials containing any type of emitter (except the ^{232}Th series which is excluded for the moment). The contribution of the ^{235}U chain is also excluded. Indeed, the proportion (in relative mass) of ^{235}U/^{238}U is 0.72 %, and for an ore at secular equilibrium the proportion of A(^{235}U)/A(^{238}U) activities is 4.59 %. The developed method to discriminate ^{226}Ra works with uncertainties mainly related to the number of particles counted (statistics). The activity must be sufficient to be able to measure a representative energy spectrum. In the selected ROIs the total number of counts in the energy spectrum ranges from 169 to 1504 (see Table 1). It is therefore important to work in "relatively large" ROIs compared to the pixel size, with appropriate acquisition times to allow sufficient counts for each ROI studied.

4.1. Homogeneous standard sample

Since the ore sample was at secular equilibrium, it was expected that the relative proportions between ^{226}Ra and the other emitters such as uranium would be identical at all points on the surface. The measured Ra/TOT map is shown in Fig. 13 (A), and the distribution of Ra/TOT ratios for each image pixel in Fig. 13 (B). This distribution is not totally gaussian and a heterogeneity in the Ra/TOT map can be observed. The linearity between the distribution of the Ra count versus the TOT count Fig. 13 (C) suggests that this heterogeneity is not due to a statistical effect, but rather the imperfection of the sample surface, as variations in its thickness induce additional charges which are measured by the detector (see (Lefeuvre et al., 2022) for details about the charge readout). Nevertheless, it is possible by distribution fitting to measure an average ratio of Ra/TOT = 0.22 corresponding to this sample, instead of an expected value of Ra/TOT = 0.24. The same observation, and the average Ra/TOT measurement of 0.28 was made for the reference sample of ^{226}Ra-doped celestine (see Supplementary S7) instead of an expected value of Ra/TOT = 0.30.

4.2. Analysis of U-mill tailing sample from bulk to mineral heterogeneities

The bulk ^{226}Ra activity (2.40 Bq) measurement on the thin section of

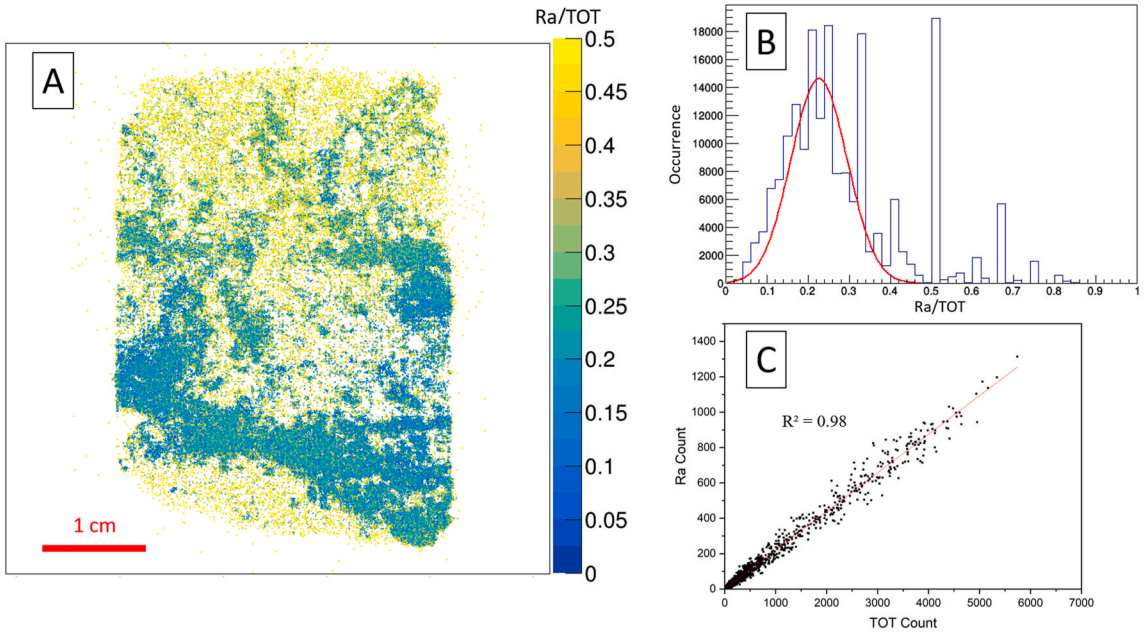

Fig. 13. Ra/TOT map for uranium ore sample (50 μm pixel size) (A), and 1D distribution of Ra/TOT pixels value of the map A (B), distribution of Ra count versus TOT count (for a larger pixel size of 800 μm) (C).

the 9693-3 sample with SA gives a mass activity of 52 Bq/g (i.e. 1.42 × 10^{-3} ppm), which is consistent with a bulk measurement by gamma spectrometry giving 55.2 Bq/g. The mapping of ^{226}Ra and more particularly the Ra/TOT map for the 9693-3 sample show localized heterogeneities of the radium distribution with respect to the ^{238}U series.

In Table 1, the ^{226}Ra contents are measured in mineral phases with sufficient gross alpha activity (barite and siderite). Thanks to the thresholding on the alpha energy spectrum measured in the ROIs, it has been clearly shown that the ^{226}Ra content differs greatly between the two phases, which are in a totally different radioactive equilibrium state. Using SA, the measurement of ^{226}Ra thanks to its daughter isotopes is consistent with a trapping of ^{226}Ra on barite. The measurements on siderite suggest the quasi-absence of ^{226}Ra in this iron carbonate, thus, the alpha activity principally comes from the uranium recently absorbed in these secondary phases. For barite, the error on the ^{226}Ra content is low as the U/Ra ratios are also low. Conversely, for siderite, the relative error on the ^{226}Ra content is certainly higher because the U/Ra ratios are high. Nevertheless, these results, when analyzed in the light of the well-known retention properties of carbonate- and sulfate-bearing minerals towards U and Ra respectively ((Ithurbide et al., 2010), (Jones et al., 2011), (Lestini et al., 2019), (Billon et al., 2024), and references therein), are consistent with a significant ^{226}Ra deficit in siderite with respect to barite.

As the 9693-3 sample is depleted in U after its chemical extraction in the mill, heterogeneities between ^{226}Ra and its alpha-decay fathers {U, Th} are to be expected. This is the case for example in ROI_1 where the heterogeneity between 1_1 and 1_2 (Fig. 9 (C)) is clearly visible in terms of the Ra/TOT ratio. As the two are spatially very close (only 830 μm apart), they can be compared because they undergo the same signal variations on the traces of the alpha particles. The distribution of the Ra/TOT ratio values for the 15 sub-ROIs analyzed on the 9693-3 sample is

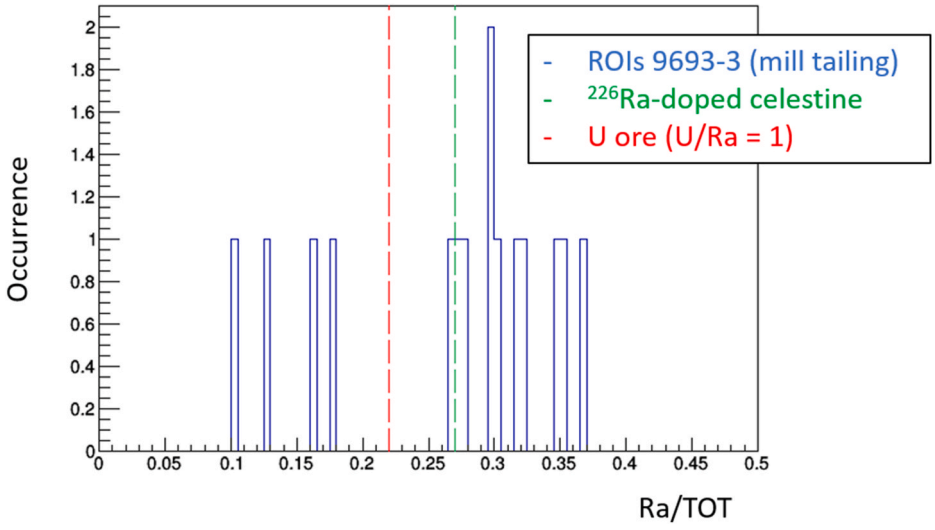

Fig. 14. Ra/TOT ratios in 9693-3 selected ROIs in blue, compared with U ore (secular equilibrium) Ra/TOT bulk ratio in red and the ^{226}Ra-doped celestine (excess of ^{226}Ra) in green.

plotted in Fig. 14 and compared with the values of the two reference sources (U ore and ^{226}Ra-doped celestine).

Four Ra/TOT values are below the ratio corresponding to secular equilibrium (line shown in red on Fig. 14): they correspond to ROIs with siderite and low ^{226}Ra activity but a high concentration of U as confirmed in Table 1 with uranium present between 0.67 % and 2.2 % measured by EDS. These enrichments are consistent with a remobilization of uranium after the ore treatment, and a subsequent retention by siderite (Ithurbide et al., 2010).

The contributions above the ore line (shown in red) on Fig. 14 are then associated with areas (see Table 1) that do not contain uranium (or negligibly, compared to the measured autoradiographic signal). There is thus an excess of ^{226}Ra. These radium-rich phases are associated with barites (see Table 1) that are well known to incorporate ^{226}Ra in the U-mining environment by means of solid solution mechanisms (Ithurbide et al., 2010) (Fernández-González et al., 2013) (Besançon, 2022) (Reymond et al., 2023) (Billon et al., 2024). These values are close to the Ra/TOT value of celestine (in green on Fig. 14) which does not contain uranium. Discrepancies with higher values may be explained by the presence in non-equilibrium of ^{226}Ra decay products.

For distant ROIs on the thin section, the Ra/TOT measurement approach also succeeds in identifying disequilibrium despite the heterogeneity highlighted with the U ore sample. It is possible to validate these findings by means of the correlation made between the mineralogy and the different Ra/TOT level of SA. The variation created by undesirable heterogeneity is less important than the variation due to a strong U/Ra >1 disequilibrium. In addition, it should be borne in mind that the comparison between autoradiography and SEM can be limited: autoradiography can detect alpha emitted from a depth of 30 μm, while SEM analysis is only effective inside the first μm of material (interaction volume between electrons probe (15 kV) and sample).

4.3. Limitations

^{222}Rn is a volatile gas generated after the radioactive decay of ^{226}Ra. This gas may escape from the sample (Baskaran, 2016) if no precaution is taken. In such a case, the equilibrium between ^{226}Ra and its daughters is not verified. In the present study, the porosity of the samples was filled with resin, which is supposed here to prevent the escape of ^{222}Rn (INTERNATIONAL ATOMIC ENERGY AGENCY, 2014). Measurement was always made more than 30 days after the manufacture of the thin sections, in order to verify the equilibrium with ^{226}Ra. Concurrently, the spectral response in alpha spectrometry is a good indicator to assess whether radon is escaping. For future developments concerning the mapping of ^{226}Ra, the determination of radon fluxes emanating from the studied samples should be assessed experimentally (Baskaran, 2016). This bulk measurement could be obtained by using solid state detectors such as polycarbonate films. The rate of emanation of ^{222}Rn depends on the local porosity of the host mineral, and the resulting radon gas diffusion properties (Hellmuth et al., 2017). A possible emanation of ^{222}Rn from the sample results in an underestimation of ^{226}Ra, mainly due to the decreased contribution of ^{214}Po to the alpha spectrum. This contribution represents the majority signal above the 5.5 MeV energy threshold used to quantify ^{226}Ra from the alpha spectrum.

The method developed here is mainly constrained by the limitation of acquisition time, but remains reasonable for a one-week-long acquisition. However, it is necessary to acquire a sufficiently large number of events to compensate for the statistical uncertainties related to the counting and the low sensitivity of the variations of the quantities that are measured for the various states of equilibrium (more particularly when U/Ra <1).

Another limitation comes from the complexity of geological matrices. The calibration of radium counting is only effective if the sample studied has the same configuration as the calibration source (grain density and thickness) to warrant the same emissions of alpha particles from minerals below the sample surface. The studied minerals in this paper exhibit the same range of density: 3.95 g/cm^3, 4.6 g/cm^3 and 3.96 g/cm^3 respectively for celestine, barite and siderite. Therefore, no significant matrix effect in the measurement is to be expected. The thickness was assumed to be 22 μm. For a better measurement of ^{226}Ra content, the density and thickness must be considered. For this, the emission fraction F_E of the radioactivity depending on these two characteristics must be taken into account in the conversion factor k_8 (5500 keV). A possible approach to measure the thickness would be the use of X-ray μ-tomography which can reach spatial resolutions of 300 nm. In addition, imperfections on the sample surface can create non-negligible artefacts for energy spectrum measurements. Preparing the thin-section sample requires precision and flatness.

Finally, we emphasize that an important perspective of this work is to better estimate the uncertainty associated with the quantitativity of the ^{226}Ra measurement using SA. This could be achieved by a detailed study of the estimation of SA error sources. These are complex and encompass various aspects related to the acquisition of the alpha spectrum itself (SA method, counting statistics, grid heterogeneity), source geometry (thickness, roughness) and radon escape. A comparison of bulk ^{226}Ra content, measured either by SA or by other existing techniques such as mass spectrometry, would also be necessary in the future.

5. Conclusions

The local measurement of ^{226}Ra naturally occurring in geo-materials using a non-destructive method was here achieved. The method used a spectroscopic autoradiography (SA) measurement which is the combination of an imaging modality and a spectroscopy modality for alpha particles. This is possible for thin-section sample analysis, using a PIM detector. A sample of a U-mill tailing was studied in detail, and it was possible to quantitatively map ^{226}Ra among other emitters such as ^{238}U. The spatial resolution of this discrimination was about 50 μm. Complementary SEM measurements were carried out to identify the carrier phases of ^{226}Ra and uranium radioactivity. By utilizing the energy spectrum of the alpha particles, an indicator on the proportions of ^{226}Ra in relation to its fathers was measured: Ra/TOT. This ratio allows us to be predictable for the measurement of so-called young uranium, which in this case study is associated with siderite. Indeed, in the sample, heterogeneities between U and Ra were observed: U can recrystallize or be trapped by retention processes in the mineral phases (clays, oxides, siderite), resulting in young uranium. Radium is preferentially trapped in barite, contents of the order of 3 ppm being measured.

From an improvement perspective, the measurement of radium is only possible if the ^{226}Ra is in equilibrium with its daughters and in particular with the ^{222}Rn. This equilibrium must be assessed, and corrected if it is not the case. In this study, the contribution solely of the ^{238}U series was considered in the samples. However to move towards an ideal measurement of ^{226}Ra in highly complex matrixes, the cases of other naturally radioactive chains such as ^{232}Th should be considered. The energies associated with this chain range from 4012 keV for ^{232}Th to 8784 keV for ^{212}Po, and secular equilibrium is reached in 57 y (10 times $T_{1/2}$ = 5.7 y for ^{228}Ra). Their presence would inevitably generate an error on the ^{226}Ra count. But a bulk study of alpha spectrometry would allow their activity to be quantified. Moreover, the alpha energy of the ^{212}Po is above the energy of ^{214}Po (^{238}U series), so a discrimination of the ^{232}Th series in the presence of the ^{238}U series could be studied directly with the SA of the PIM detector.

CRediT authorship contribution statement

Hugo Lefeuvre: Writing – review & editing, Writing – original draft, Software, Methodology, Investigation, Formal analysis, Data curation, Conceptualization. **Sophie Billon:** Writing – review & editing, Writing – original draft, Validation, Supervision, Methodology, Investigation, Formal analysis, Data curation. **Michael Descostes:** Writing – original draft, Validation, Supervision, Project administration, Formal analysis,

Conceptualization. **Jérôme Donnard:** Writing – original draft, Supervision, Project administration, Methodology, Funding acquisition, Formal analysis, Conceptualization. **Samuel Duval:** Writing – original draft, Supervision, Methodology, Formal analysis. **Paul Sardini:** Writing – review & editing, Writing – original draft, Validation, Supervision, Project administration, Methodology, Funding acquisition, Formal analysis, Conceptualization.

Declaration of competing interest

The authors declare that they have no known competing financial interests or personal relationships that could have appeared to influence the work reported in this paper.

Data availability

Data will be made available on request.

Acknowledgments

This work has been done within the framework of a CIFRE Ph. D thesis (n°2020/0166) agreement between the University of Poitiers, CNRS, ERM (SARL) (Poitiers, France), Orano Mining and ANRT. We would like to thank Julie Champion from Subatech Laboratory for her valuable assistance for the spectroscopy measurements.

Appendix A. Supplementary data

Supplementary data to this article can be found online at https://doi.org/10.1016/j.jenvrad.2024.107392.

References

Ahmad, F., Morris, K., Law, G.T.W., Taylor, K.G., Shaw, S., 2021. Fate of radium on the discharge of oil and gas produced water to the marine environment. Chemosphere 273, 129550. https://doi.org/10.1016/j.chemosphere.2021.129550.

Angileri, A., Sardini, P., Donnard, J., Duval, S., Lefeuvre, H., Oger, T., Patrier, P., Rividi, N., Siitari-Kauppi, M., Toubon, H., Descostes, M., 2018. Mapping ^{238}U decay chain equilibrium state in thin sections of geo-materials by digital autoradiography and microprobe analysis. Appl. Radiat. Isot. 140, 228–237. https://doi.org/10.1016/j.apradiso.2018.06.018.

Angileri, A., Sardini, P., Beaufort, D., Amiard, G., Beaufort, M.F., Nicolai, J., Siitari-Kauppi, M., Descostes, M., 2020. Mobility of daughter elements of ^{238}U decay chain during leaching by in Situ Recovery (ISR): new insights from digital autoradiography. J. Environ. Radioact. 220–221, 106274 https://doi.org/10.1016/j.jenvrad.2020.106274.

Baetslé, L., 1991. Study of the Radionuclides Contained in Wastes Produced by the Phosphate Industry and Their Impact on the Environment. European Commission, Publications Office.

Ballini, M., Chautard, C., Nos, J., Phrommavanh, V., Beaucaire, C., Besançon, C., Boizard, A., Cathelineau, M., Peiffert, C., Vercouter, T., Vors, E., Descostes, M., 2020. A multi-scalar study of the long-term reactivity of uranium mill tailings from Bellezane site (France). J. Environ. Radioact. 218, 106223 https://doi.org/10.1016/j.jenvrad.2020.106223.

Baskaran, M., 2016. Radon: A Tracer for Geological, Geophysical and Geochemical Studies. Springer International Publishing, Cham. https://doi.org/10.1007/978-3-319-21329-3.

Becker, J.S., 2003. Mass spectrometry of long-lived radionuclides. Spectrochim. Acta B Atom Spectrosc. 58, 1757–1784. https://doi.org/10.1016/S0584-8547(03)00156-3.

Besançon, C., 2022. Study of ^{226}Ra Mobility in Natural Man-Influenced Environments through Experimental Approaches and Geochemical Modelling, Phd Thesis. Sorbonne Université. https://theses.hal.science/tel-03715389. May 11, 2023.

Besançon, C., Sardini, P., Savoye, S., Descostes, M., Gérard, M., 2022. Quantifying ^{226}Ra activity in a complex assemblage of ^{226}Ra-bearing minerals using alpha autoradiography and SEM/EDS. J. Environ. Radioact. 251–252, 106951 https://doi.org/10.1016/j.jenvrad.2022.106951.

Billon, S., Sardini, P., Leblond, S., Fichet, P., 2019. From Bq cm^{-3} to Bq cm^{-2} (and conversely)—part 1: a useful conversion for autoradiography. J. Radioanal. Nucl. Chem. 320, 643–654. https://doi.org/10.1007/s10967-019-06521-w.

Billon, S., Sardini, P., Angileri, A., Beaucaire, C., Parneix, J.C., Siitari-Kauppi, M., Descostes, M., 2020. Quantitative imaging of ^{226}Ra ultratrace distribution using digital autoradiography: case of doped celestines. J. Environ. Radioact. 217, 106211 https://doi.org/10.1016/j.jenvrad.2020.106211.

Billon, S., Savoye, S., Sardini, P., Gérard, M., Beaucaire, C., Descostes, M., 2024. Sequential extractions versus alpha autoradiography: mutually complementary for the identification of U- and Ra-bearing minerals in mine tailings. J. Geochem. Explor. 257, 107368 https://doi.org/10.1016/j.gexplo.2023.107368.

Bordelet, G., Beaucaire, C., Phrommavanh, V., Descostes, M., 2018. Chemical reactivity of natural peat towards U and Ra. Chemosphere 202, 651–660. https://doi.org/10.1016/j.chemosphere.2018.03.140.

Chautard, C., Beaucaire, C., Gerard, M., Roy, R., Savoye, S., Descostes, M., 2020. Geochemical characterization of uranium mill tailings (Bois Noirs Limouzat, France) highlighting the U and ^{226}Ra retention. J. Environ. Radioact. 218, 106251 https://doi.org/10.1016/j.jenvrad.2020.106251.

Cocherie, A., Legendre, O., Peucat, J.J., Kouamelan, A.N., 1998. Geochronology of polygenetic monazites constrained by in situ electron microprobe Th-U-total lead determination: implications for lead behaviour in monazite. Geochem. Cosmochim. Acta 62, 2475.

Çubukçu, H.E., Ersoy, O., Aydar, E., Çakir, U., 2008. WDS versus silicon drift detector EDS: a case report for the comparison of quantitative chemical analyses of natural silicate minerals. Micron 39, 88–94. https://doi.org/10.1016/j.micron.2006.11.004.

de Boissezon, H., Levy, L., Jakymiw, C., Distinguin, M., Guerin, F., Descostes, M., 2020. Modeling uranium and 226Ra mobility during and after an acidic in situ recovery test (Dulaan Uul, Mongolia). J. Contam. Hydrol. 235, 103711 https://doi.org/10.1016/j.jconhyd.2020.103711.

Déjeant, A., Bourva, L., Sia, R., Galoisy, L., Calas, G., Phrommavanh, V., Descostes, M., 2014. Field analyses of 238U and 226Ra in two uranium mill tailings piles from Niger using portable HPGe detector. J. Environ. Radioact. 137, 105–112. https://doi.org/10.1016/j.jenvrad.2014.06.012.

Donnard, J., Arlicot, N., Berny, R., Carduner, H., Leray, P., Morteau, E., Servagent, N., Thers, D., 2009a. Advancements of labelled radio-pharmaceutics imaging with the PIM-MPGD. J. Inst. Met. 4, P11022. https://doi.org/10.1088/1748-0221/4/11/P11022. P11022.

Donnard, J., Berny, R., Carduner, H., Leray, P., Morteau, E., Provence, M., Servagent, N., Thers, D., 2009b. The micro-pattern gas detector PIM: a multi-modality solution for novel investigations in functional imaging. Nucl. Instrum. Methods Phys. Res. Sect. A Accel. Spectrom. Detect. Assoc. Equip. 610, 158–160. https://doi.org/10.1016/j.nima.2009.05.186.

Donnard, J., Thers, D., Servagent, N., Luquin, L., 2009c. High spatial resolution in β-imaging with a PIM device. IEEE Trans. Nucl. Sci. 56, 197–200. https://doi.org/10.1109/TNS.2008.2005673.

Fayek, M., Janeczek, J., Ewing, R.C., 1997. Mineral chemistry and oxygen isotopic analyses of uraninite, pitchblende and uranium alteration minerals from the Cigar Lake deposit, Saskatchewan, Canada. Appl. Geochem. 12, 549–565. https://doi.org/10.1016/S0883-2927(97)00032-2.

Fernández-González, A., Carneiro, J., Katsikopoulos, D., Prieto, M., 2013. Thermodynamic properties of the (Ba,Pb)SO_4 solid solution under ambient conditions: implications for the behavior of Pb and Ra in the environment. Geochem. Cosmochim. Acta 105, 31–43. https://doi.org/10.1016/j.gca.2012.11.042.

Hellmuth, K.H., Siitari-Kauppi, M., Arvela, H., Lindberg, A., Fonteneau, L., Sardini, P., 2017. Radon emanation from fresh, altered and disturbed granitic rock characterized by 14C-PMMA impregnation and autoradiography. Appl. Radiat. Isot. 127, 195–208.

Hou, X., Roos, P., 2008. Critical comparison of radiometric and mass spectrometric methods for the determination of radionuclides in environmental, biological and nuclear waste samples. Anal. Chim. Acta 608, 105–139. https://doi.org/10.1016/j.aca.2007.12.012.

ImageJ. Image processing and analysis in java. https://imagej.nih.gov/ij/. January 17, 2023).

INTERNATIONAL ATOMIC ENERGY AGENCY, 2004. Application of the Concepts of Exclusion, Exemption and Clearance. IAEA, Vienna. Safety Standards Series No. RS-G-1.7. https://www.iaea.org/publications/7118/application-of-the-concepts-of-exclusion-exemption-and-clearance.

INTERNATIONAL ATOMIC ENERGY AGENCY, 2010. Handbook of Parameter Values for the Prediction of Radionuclide Transfer in Terrestrial and Freshwater Environments. IAEA, Vienna. Technical Reports Series No. 472.

INTERNATIONAL ATOMIC ENERGY AGENCY, 2014. The Environmental Behaviour of Radium: Revised Edition. IAEA, Vienna. Technical reports series No. 476. https://www.iaea.org/publications/10478/the-environmental-behaviour-of-radium-revised-edition. February 23, 2023.

Ithurbide, A., Peulon, S., Miserque, F., Beaucaire, C., Chaussé, A., 2010. Retention and redox behaviour of uranium(VI) by siderite. $FeCO_3$) 98, 563–568. https://doi.org/10.1524/ract.2010.1754.

Jirásek, J., Matýsek, D., Alexa, P., Osovský, M., Uhlář, R., Sivek, M., 2020. High specific activity of radium isotopes in baryte from the Czech part of the upper silesian basin—an example of spontaneous mine water treatment. Minerals 10, 103. https://doi.org/10.3390/min10020103.

Jones, M.J., Butchins, L.J., Charnock, J.M., Pattrick, R.A.D., Small, J.S., Vaughan, D.J., Wincott, P.L., Livens, F.R., 2011. Reactions of radium and barium with the surfaces of carbonate minerals. Appl. Geochem. 26, 1231–1238. https://doi.org/10.1016/j.apgeochem.2011.04.012.

Klinkenberg, M., Brandt, F., Breuer, U., Bosbach, D., 2014. Uptake of Ra during the recrystallization of barite: a microscopic and time of flight-secondary ion mass spectrometry study. Environ. Sci. Technol. 48, 6620–6627. https://doi.org/10.1021/es405502e.

Kollmer, F., Paul, W., Krehl, M., Niehuis, E., 2013. Ultra high spatial resolution SIMS with cluster ions — approaching the physical limits. Surf. Interface Anal. 45, 312–314. https://doi.org/10.1002/sia.5093.

Leermakers, M., Phrommavanh, V., Drozdzak, J., Gao, Y., Nos, J., Descostes, M., 2016. DGT as a useful monitoring tool for radionuclides and trace metals in environments impacted by uranium mining: case study of the Sagnes wetland in France. Chemosphere 155, 142–151. https://doi.org/10.1016/j.chemosphere.2016.03.138.

Lefeuvre, H., Donnard, J., Descostes, M., Billon, S., Duval, S., Oger, T., Toubon, H., Sardini, P., 2022. Spectroscopic autoradiography of alpha particles using a parallel ionization multiplier gaseous detector. Nucl. Instrum. Methods Phys. Res. Sect. A Accel. Spectrom. Detect. Assoc. Equip. 1035, 166807 https://doi.org/10.1016/j.nima.2022.166807.

Lestini, L., Beaucaire, C., Vercouter, T., Ballini, M., Descostes, M., 2019. Role of trace elements in the 226-radium incorporation in sulfate minerals (gypsum and celestite). ACS Earth Space Chem. 3, 295–304. https://doi.org/10.1021/acsearthspacechem.8b00150.

McGee, J.J., Keil, K., 2001. Application of electron probe microanalysis to the study of geological and planetary materials. Microsc. Microanal. 7, 200–210. https://doi.org/10.1007/S100050010081.

Mvondo, S., Ben-Bolie, G.H., Ema'a, J.M.E., Ateba, P.O., Ele abiama, P., Ateba, J.F.B., 2017. Study of soil-fern transfer of naturally occurring alpha emitting radionuclides in the Southern Region of Cameroon. J. Environ. Radioact. 180, 114–119. https://doi.org/10.1016/j.jenvrad.2017.10.007.

PIPS® Detectors Passivated Implanted Planar Silicon Detectors, Mirion. https://www.mirion.com/products/technologies/spectroscopy-scientific-analysis/research-education-and-industrial-solutions/passivated-implanted-planar-silicon-pips-detectors/standard-pips-detectors/pips-detectors-passivated-implanted-planar-silicon-detectors (accessed July 31, 2023).

Reymond, M., Descostes, M., Besançon, C., Leermakers, M., Billon, S., Cherfallot, G., Muguet, M., Beaucaire, C., Smolikova, V., Patrier, P., 2023. Assessment of 226Ra and U colloidal transport in a mining environment. Chemosphere, 139497.

Robin, V., Tertre, E., Beaucaire, C., Regnault, O., Descostes, M., 2017. Experimental data and assessment of predictive modeling for radium ion-exchange on beidellite, a swelling clay mineral with a tetrahedral charge. Appl. Geochem. 85, 1–9. https://doi.org/10.1016/j.apgeochem.2017.07.009.

Rollog, M., Cook, N.J., Guagliardo, P., Ehrig, K., Kilburn, M., 2020. Radionuclide distributions in Olympic Dam copper concentrates: the significance of minor hosts, incorporation mechanisms, and the role of mineral surfaces. Miner. Eng. 148, 106176 https://doi.org/10.1016/j.mineng.2019.106176.

Sardini, P., Angileri, A., Descostes, M., Duval, S., Oger, T., Patrier, P., Rividi, N., Siitari-Kauppi, M., Toubon, H., Donnard, J., 2016. Quantitative autoradiography of alpha particle emission in geo-materials using the Beaver^{TM} system. Nucl. Instrum. Methods Phys. Res. Sect. A Accel. Spectrom. Detect. Assoc. Equip. 833, 15–22. https://doi.org/10.1016/j.nima.2016.07.003.

Siiskonen, T., Pöllänen, R., 2005. Advanced simulation code for alpha spectrometry. Nucl. Instrum. Methods Phys. Res. Sect. A Accel. Spectrom. Detect. Assoc. Equip. 550, 425–434. https://doi.org/10.1016/j.nima.2005.05.045.

Song, K., Park, J.-H., Lee, C.-G., Han, S.-H., 2016. Recent developments in nuclear forensic and nuclear safeguards analysis using mass spectrometry. Mass Spectrometry Letters 7, 31–40. https://doi.org/10.5478/MSL.2016.7.2.31.

Thakur, P., Ward, A.L., González-Delgado, A.M., 2021. Optimal methods for preparation, separation, and determination of radium isotopes in environmental and biological samples. J. Environ. Radioact. 228, 106522 https://doi.org/10.1016/j.jenvrad.2020.106522.

Tinker, R., Smith, J., Cooper, M., 1995. An assessment of the selection criteria for an analytical method for radium-226 in environmental samples. J. Radioanal. Nucl. Chem. 193, 329–336. https://doi.org/10.1007/bf02039890.

UNSCEAR, 2010. Sources and Effects of Ionizing Radiation: United Nations Scientific Committee on the Effects of Atomic Radiation: UNSCEAR 2008 Report to the General Assembly, with Scientific Annexes A and B. United Nations, New York. https://www.unscear.org/unscear/en/publications/2008_1.html.

World Health Organization, 1993. Guidelines for Drinking-Water Quality: Volume 1: Recommendations, second ed. World Health Organization https://apps.who.int/iris/handle/10665/259956. January 16, 2023).